ACS APPLIED MATERIALS & INTERFACES

Research Article

www.acsami.org

Understanding the Role of Few-Layer Graphene Nanosheets in Enhancing the Hydrogen Sorption Kinetics of Magnesium Hydride

Guang Liu,[‡] Yijing Wang,*[,†] Lifang Jiao,[†] and Huatang Yuan[†]

[†]Institute of New Energy Material Chemistry, Key Laboratory of Advanced Energy Materials Chemistry (MOE), Collaborative Innovation Center of Chemical Science and Engineering (Tianjin), Tianjin Key Lab on Metal and Molecule-based Material Chemistry, Nankai University, Tianjin 300071, P. R. China

[‡]Research Institute of Special Chemicals, Taiyuan University of Technology, Taiyuan 030024, Shanxi, P. R. China

Supporting Information

ABSTRACT: The catalytic effects of few-layer, highly wrinkled graphene nanosheet (GNS) addition on the dehydrogenation/rehydrogenation performance of MgH_2 were investigated. It was found that MgH_2−5 wt %GNSs nanocomposites prepared by ball milling exhibit relatively lower sorption temperature, faster sorption kinetics, and more stable cycling performance than that of pure-milled MgH_2. The dehydrogenation step confirms that the Avrami exponent *n* increases from 1.22 to 2.20 by the Johnson−Mehl−Avrami (JMA) formalism when the desorption temperature is reduced from 350 °C to 320 °C and 300 °C, implying that a change in the decomposition temperature can alter the mechanism during the dehydrogenation process. For rehydrogenation, the Avrami value *n* is close to 1; further study by several models coincident with $n = 1$ reveals that the absorption process of the MgH_2−5 wt %GNSs sample conforms to the Mampel equation formulated through the random nucleation approach and that the nature of the absorption mechanism does not change within the temperature range studied. Furthermore, microstructure analysis demonstrated that the defective GNSs are distributed uniformly among the MgH_2 particles and that the grain size of the MgH_2−5 wt %GNSs nanocomposite is approximately 5−9 nm. The efficient metal-free catalytic dehydrogenation/rehydrogenation of MgH_2 can be attributed to the coupling of the nanosize effect and defective GNSs.

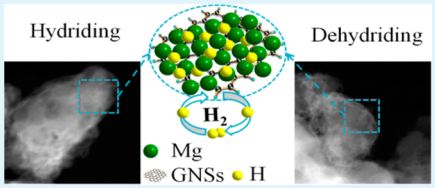

KEYWORDS: *hydrogen storage, magnesium hydride, dehydrogenation/rehydrogenation, graphene nanosheets, catalytic effects, modeling study*

1. INTRODUCTION

Contrasting its high elemental abundance, eco-friendly nature, and maximum energy content per unit weight with any non-nuclear fuel,[1,2] hydrogen is considered as a kind of green energy for fuel cell devices and vehicles for the future. The largest challenge remaining in its implementation is lack of an efficient hydrogen storage system that must be compact and safe. To find the most optimal hydrogen storage materials,[3−5] numerous studies have been carried out. As potential hydrogen storage materials, MgH_2 has generated great interest because of a high volumetric capacity of 110 g/L, a high gravimetric capacity of 7.6 wt %, low cost, earth abundance, and high safety.[6,7] However, the sluggish kinetics and high operating temperature for hydrogen absorption/desorption limit the practical use of MgH_2.

For improving the hydrogen storage properties of MgH_2, numerous strategies such as catalyzing, alloying, and nanoscaling[8−13] have been developed. The strategy of ball-milled MgH_2 with various carbon materials[14−19] has been proved to be successful in promoting the dehydrogenation/rehydrogenation kinetics as well as lowering the dehydrogenation/rehydrogenation temperature. Wu et al.[16] investigated the carbon additives (graphite, activation carbon, carbon black, C_{60}, and SWCNTs), which exhibited prominent advantages over noncarbon (BN nanotubes and asbestos) additives in accelerating the sorption kinetics and hydrogen storage capacity of MgH_2. SWCNTs exhibited the most positive effects on the hydrogen storage behavior of MgH_2 among these carbon additives. It was speculated that incorporation of a novel microstructure for the SWCNTs, which are long cylinders with a typical diameter of 1−2 nm, increases the hydrogen diffusion driving force and grain boundary. Similarly, the decomposition effects of various carbon materials including activated carbon, activated carbon fibers, graphite, MWCNTs, and carbon nanofibers (CNFs) on MgH_2 were reported.[17] It was shown that the hydrogen-desorbed temperature of these mixtures was decreased and the mixed MWCNT and CNF composites with Ni or Fe impurities had the best results. It was also shown that the enhancement of decomposition can be ascribed to the presence of carbon materials, which prevented MgH_2 particle growth. Early work performed by Imamura et al.[14,20−22] has demonstrated that the hydrogenation of the Mg−graphite nanocomposite was improved by ball milling with different organic additives, and it was indicated that highly dispersed cleavage-degraded graphite with nanosize acts as an active site for uptake and

Received: October 7, 2013
Accepted: June 18, 2014
Published: June 18, 2014

 © 2014 American Chemical Society

release of hydrogen during the dehydrogenation/rehydrogenation process.

On the other hand, graphene, a single-layer or few-layer carbon network derived from graphite, has attracted extensive attention due to its amazing properties.[23,24] Owing to its excellent mechanical, electronic, chemical, and structural properties, such as surface area, pore geometry, and active edge sites, continuous scientific studies have been directed toward promising applications of graphene including energy storage/conversion,[25−27] catalysis,[28−30] and nanoelectronics.[31−33] In our recent work, we reported the synergistic effect of graphene nanosheets (GNSs) decorated with transitional metal or transitional compounds on improving the hydrogen storage behavior and kinetics of MgH_2,[34,35] and we also reported the effects of highly crumpled GNSs toward the dehydrogenation/rehydrogenation of MgH_2.[36] It was confirmed that GNSs with crumpled structure exhibited a favorable effect on hydrogen storage performance. Therefore, the voluminal and kinetic improvements in the initial dehydrogenation/rehydrogenation performance of the MgH_2−GNSs system are well accepted results, but the dehydrogenation/rehydrogenation mechanism and the function of catalytic GNSs through the dehydrogenation/rehydrogenation cycles have not received much attention.

Herein we report an integrated investigation of thermodynamics, kinetics, and microstructures for MgH_2 dehydrogenation/rehydrogenation that can help to clarify the dehydrogenation/rehydrogenation mechanism and explain the catalytic effects of GNSs during the dehydrogenation/rehydrogenation cycles. Elucidation of the fundamental mechanism responsible for the enhanced hydrogen sorption properties of the MgH_2−GNSs system may lead to the design and development of modified Mg-based hydrogen storage materials.

2. EXPERIMENTAL SECTION

2.1. Chemicals. GNSs were synthesized by thermal exfoliation of graphene oxide (GO) at 900 °C under Ar−H_2 (9:1 by volume ratio) flow for 30 min in a quartz tube. Then 5 wt % as-prepared GNSs were mixed with MgH_2 (Alfa Aesar, 98%) powder, and then the mixtures were mechanically milled to obtain MgH_2−5 wt %GNSs (denoted as MgH_2−5GNSs) as follows: powder-to-ball mass ratio equal to 1:40, 0.5 MPa pressure of hydrogen, rotational speed of 450 rpm, milling time of 20 h. To avoid H_2O and O_2 contamination, a glovebox purified with purified argon (99.999%) was also employed for handling all the materials.

2.2. Characterizations. Powder X-ray diffraction (XRD) was performed by using a Rigaku MiniFlexII with Cu Kα radiation. The Raman spectrum was recorded by using a Renishaw inVia with excitation at 514.5 nm. The electronic states of GNSs were measured by employing a PHI 5000 Versaprobe X-ray photoelectron spectrometer (XPS). The surface microstructural analyses were obtained with a JEOL JEM-2010FEF transmission electron microscope (TEM) and an FEI Tecnai 20 scanning microscope (STEM), which were equipped with an energy-dispersive X-ray spectrometer (EDS).

The hydrogen desorption temperature and H_2 desorption amount of MgH_2−5GNSs were characterized by using a Tianjin Golden Eagle Technology PX200 temperature-programmed desorption (TPD) system, and the analysis was performed by using a high-purity argon (99.999%) flow rate of 35.1 mL min^{-1} and 5 °C/min heating rate. A homemade Sievert's apparatus was employed to measure the absorption/desorption properties of materials, the initial rehydrogenation pressure was 2 MPa, and dehydrogenation pressure was 5 kPa, respectively. For pressure−composition−isothermal (PCI) experiments, a stainless steel reactor loaded with a 0.1−0.2 g sample was sealed in a glovebox filled with argon. The pressure value for PCI tests ranged from 0.001 to 3 MPa hydrogen (99.999%), and the temperature was set at 300 °C, 320 °C, 340 °C.

3. RESULTS

3.1. Characterization of As-Prepared GNSs. The microstructure of the GNSs was observed by TEM (Figure 1a). Most of the sheets aggregated into thicker flakes, showing a distinct wrinkle structure. Unlike the flakes that mechanically exfoliated from highly ordered graphite, these sheets aggregated in a disordered manner; thus, on the periphery of these flakes, individual graphene about three layers thick are visible. Six-fold-symmetry arc spots (002) match those expected for graphene nanosheets (for the SAED pattern of GNSs, see the inset of Figure 1a), which further confirms the disordered nature of the GNSs. XPS measurement was also employed to investigate the chemical composition of the as-prepared GNSs (Figure 1b−d). As shown in Figure 1b, there are two peaks at around 284.5 and 532 eV that correspond with the C 1s and O 1s spectrum. The results of high resolution C 1s and O 1s XPS peak-fitting clearly show C−O and C═O peaks besides sp^2-hydridized C−C (Figure 1c,d), indicating different types of doped O in the GNSs. The chemical compositions of GNSs derived from the XPS results imply that there are 93.3 wt % C and 6.7 wt % O in the GNSs, which were corrected by using the different photoionization cross sections of C 1s and O 1s.

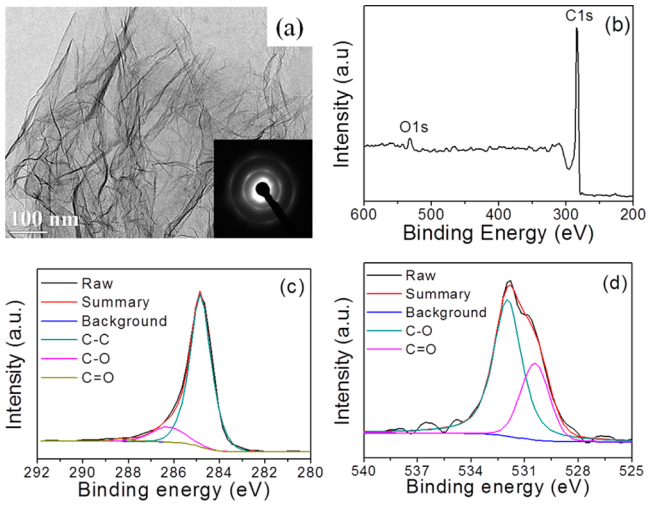

Figure 1. (a) TEM image of GNSs; the inset of panel a is the SAED pattern of GNSs. (b) Survey XPS spectra and (c) C 1s and (d) O 1s XPS spectra of GNSs.

3.2. Hydrogen Storage Properties. The thermodynamics of the MgH_2−5GNSs system was determined by pressure−composition−isothermal (PCI) experiments. The dehydrogenation reaction enthalpy was calculated by carrying out PCI runs at 300 °C, 320 °C, and 340 °C, as shown in Figure 2. The desorption curves at the corresponding temperatures of 300 °C, 320 °C, and 340 °C gave three different flat plateaus at pressures of 0.177, 0.302, and 0.485 MPa, respectively. The equilibrium pressures obtained during the desorption processes can serve to estimate the reaction enthalpy by the Van't Hoff principle as follows:

$$\ln P = \frac{\Delta H}{RT} - \frac{\Delta S}{R} \quad (1)$$

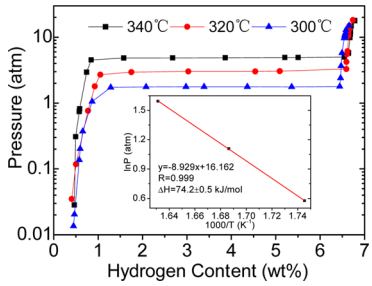

Figure 2. Pressure−composition−isothermal curves of the milled MgH_2−5GNSs at different temperatures. The inset is the Van't Hoff plot of the milled MgH_2−5GNSs derived from the dehydrogenation PCI measurements.

Therefore, the enthalpy of the MgH_2−5GNSs composites is determined to be 74.2 ± 0.5 kJ/mol H_2 from the Van't Hoff plot (the inset of Figure 2), which agrees with the standard value for MgH_2 (74.5 kJ/mol H_2),[37] proving that the enhanced hydrogenation and dehydrogenation properties are due to enhanced kinetics rather than a change in the thermodynamics.

TPD measurement was also introduced to investigate the hydrogen storage behavior of MgH_2−5GNSs and MgH_2, as shown in Figure 3. Compared to the pure-milled MgH_2, both

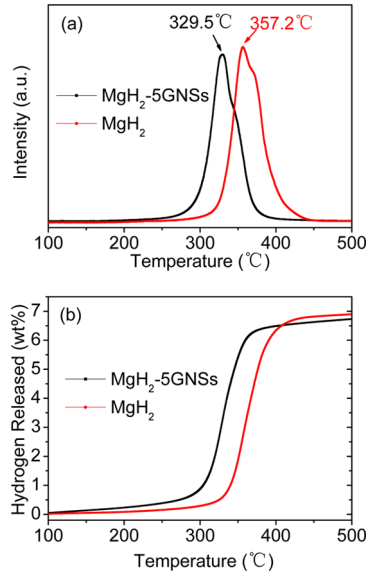

Figure 3. TPD curves of (a) peak temperature and (b) hydrogen decomposition capacity for MgH_2 and MgH_2−5GNSs composites.

the onset and peak temperature of the MgH_2−5GNSs composites are decreased (Figure 3a). The dehydrogenation temperature of MgH_2−5GNSs composites starts from ∼267 °C, 35 °C lower than that of pure MgH_2. The dehydrogenation peak temperature of MgH_2−5GNSs is around 329.5 °C, about 28 °C lower compared to 357.2 °C for pure MgH_2. This suggests that the dehydrogenation kinetics of MgH_2 can be enhanced by being ball milled with GNSs. The amount of H_2 released in the TPD characterization (see the details of Notes on Calibration and Conversion of TPD Intensity to Weight of Hydrogen in Supporting Information) is also displayed in Figure 3b. A weight of 6.73 wt % H_2 was released from MgH_2−5GNS during heating, and the onset temperature of MgH_2−5GNSs is obviously reduced compared with that for pure MgH_2 though the amount of hydrogen desorbed is slightly lower than that of pure MgH_2 due to addition of GNSs.

Besides TPD, the sorption kinetics of MgH_2−5GNSs was further investigated by isothermal dehydrogenation/rehydrogenation curves at different temperatures. As shown in Figure 4a,

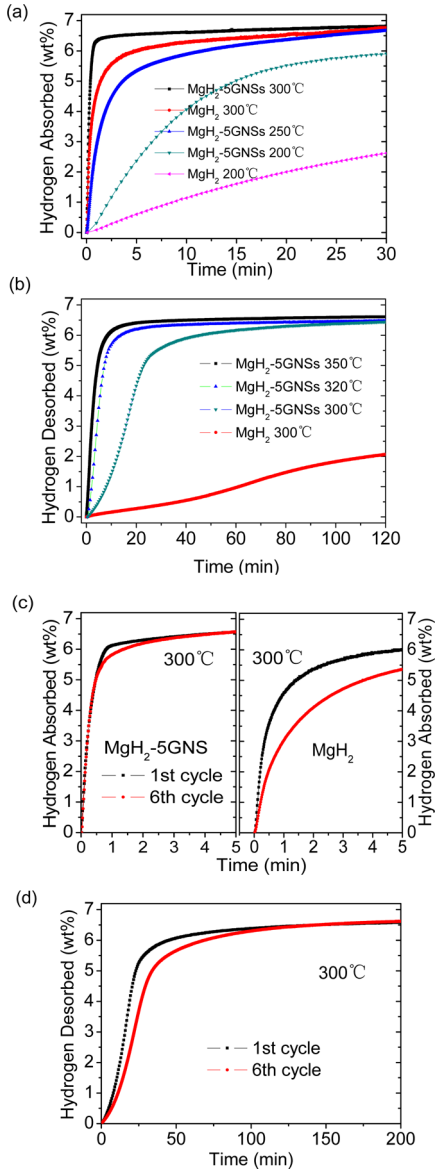

Figure 4. Rehydrogenation/dehydrogenation and cycling stability of MgH_2−5GNSs composite compared with MgH_2: (a) rehydrogenation at different temperatures under a pressure of 2 MPa; (b) dehydrogenation at different temperatures under a pressure of 5 kPa; (c) rehydrogenation cycling stability of MgH_2−5GNSs compared with MgH_2; (d) dehydrogenation cycling stability of MgH_2−5GNSs at 300 °C.

at 300 °C, the MgH_2−5GNSs composites can absorb 6.6 wt % H_2 within 1 min. When lowering the temperature to 250 °C, 6.38 wt % H_2 can be absorbed within 20 min. It can also absorb 5.91 wt % within 30 min even at 200 °C. In contrast, for pure-milled MgH_2, there is only 4.95 wt % hydrogen absorbed within 1 min at 300 °C, and only 2.62 wt % within 30 min at 200 °C. For dehydrogenation of MgH_2−5GNSs composites, 6.5 wt % H_2 can be released at 350 °C within 15 min. At 320 °C, 6.3 wt % hydrogen can be released within 30 min. When the

dx.doi.org/10.1021/am502755s | ACS Appl. Mater. Interfaces 2014, 6, 11038−11046

temperature is lowered to 300 °C, the same amount of hydrogen is still released within 80 min, as shown in Figure 4b. Cyclic stability of rehydrogenation and dehydrogenation at 300 °C were also carried out to study the cyclic kinetics of the milled MgH_2−5GNS system. Figure 4c compares the hydrogenation kinetics of MgH_2−5GNS composite and pure-milled MgH_2. There is no difference in hydrogen storage capacity and only a little slower absorption kinetics after six cycles. Furthermore, the cyclic kinetics for dehydrogenation after six cycles also exhibits the same performance, as shown in Figure 4d. In contrast, the pure-milled MgH_2 shows an obvious loss in absorption capacity and much slower absorption kinetics after six cycles. Therefore, all of the above measurements for rehydrogenation and dehydrogenation indicate that GNS additives are significantly beneficial for the hydrogen storage performance of MgH_2.

The improved kinetics of rehydrogenation and dehydrogenation was further demonstrated by the Johnson−Mehl−Avrami (JMA) model and Arrhenius analysis by fitting the absorption and desorption curves of MgH_2. The JMA model is broadly employed to interpret the time-dependent kinetics of isothermal solid−gas reaction, which can also enable characterization of the kinetic rate-limiting step and dimensionality of MgH_2/Mg phase formation. The experimental data in Figure 4a,b can be well fitted by the JMA model as follows:[38,39]

$$kt = [-\ln(1 - \alpha)]^{1/n} \quad (2)$$

Here k is the constant of reaction rate, α is the time-dependent mass fraction of reaction, and the Avrami exponent n is generally used to understand the dimensionality of the MgH_2/Mg growth process and speculate about the dehydrogenation/rehydrogenation mechanism.[40] Plotting $\ln[-\ln(1 - \alpha)]$ against $\ln t$ in the range $0.2 \leq \alpha \leq 0.8$ yields a straight line (Figure 5), where n = slope and $k = e^{(y\text{-intercept})/\text{slope}}$. It is obvious that $\ln[-\ln(1 - \alpha)]$ shifts linearly versus $\ln t$ very well ($R^2 > 0.9966$) for both the plots of rehydrogenation (Figure 5a) and dehydrogenation (Figure 5b), which indicates that the JMA model is very suitable for the determination of dehydrogenation/rehydrogenation of MgH_2−5GNSs. The data of kinetics characterized by linear fitting are also listed in Tables 1 and 2.

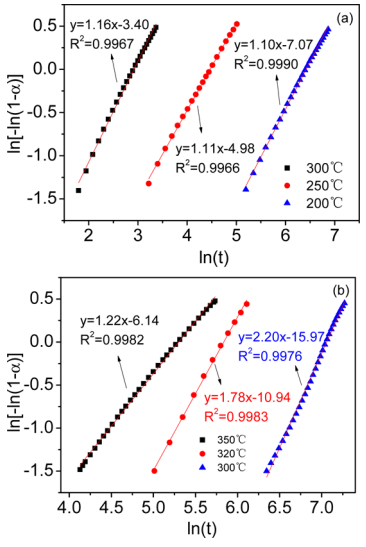

Figure 5. JMA plots for the isothermal reactions of MgH_2−5GNSs: (a) rehydrogenation and (b) dehydrogenation.

Table 1. Kinetic Data for Rehydrogenation of MgH_2−5GNSs

temperature (°C)	slope (n)	−ln k	k(× 10^{-3} s^{-1})
300	1.16	2.931	53.3
250	1.11	4.485	11.3
200	1.10	6.427	1.62

Table 2. Kinetic Data for Dehydrogenation of MgH_2−5GNSs

temperature (°C)	slope (n)	−ln k	k(× 10^{-4} s^{-1})
350	1.22	5.028	65.5
320	1.78	6.153	21.3
300	2.20	7.261	7.02

For determining the activation energies (E_a) through the Arrhenius equation, the k values were corrected by temperature T and pressure P. Hence, the Arrhenius equation can be interpreted as follows:[41]

$$k = k(P)k(T) = k(P)K_0 \exp\left(-\frac{E_a}{RT}\right) \quad (3)$$

Here $k(P)$ follows a parabolic relationship $1 - (P/P_{eq})^{1/2}$ for absorption and $1 - (P_{eq}/P)^{1/2}$ for desorption. P is the H_2 pressure during the reaction, and P_{eq} is the H_2 pressure of equilibrium. R serves as the gas constant, and E_a is the activation energy. Therefore, from absorption and desorption data, the E_a for rehydrogenation and dehydrogenation of MgH_2−5GNSs was calculated to be 78.4 and 129.2 kJ/mol (Figure 6), respectively. The value for rehydrogenation is much

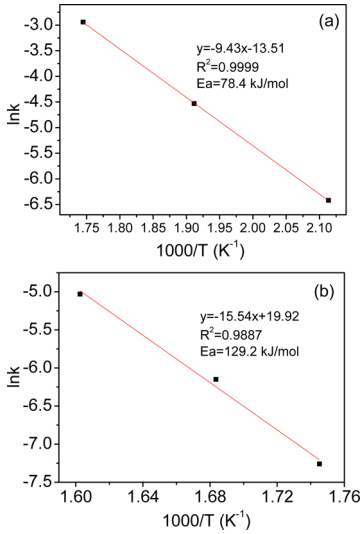

Figure 6. Arrhenius plots for the (a) rehydrogenation and (b) dehydrogenation of MgH_2−5GNSs.

lower than that of undoped sample (E_a of rehydrogenation: 99.0 kJ/mol),[36] and the dehydrogenation value is also lower than the value reported in the literature (E_a of dehydrogenation: 158.5 kJ/mol).[42]

For rehydrogenation, the Avrami value is $n \approx 1$ (Figure 5a and Table 1). It is noteworthy that there exists numerous explanations that agree with n ≈ 1, such as surface-controlled reactions, interface-controlled reactions, n-d nucleation and growth reactions, and the Mampel equation.[12,38,39,43,44] It is also notable that the MgH_2 phase growth along with 1D lines

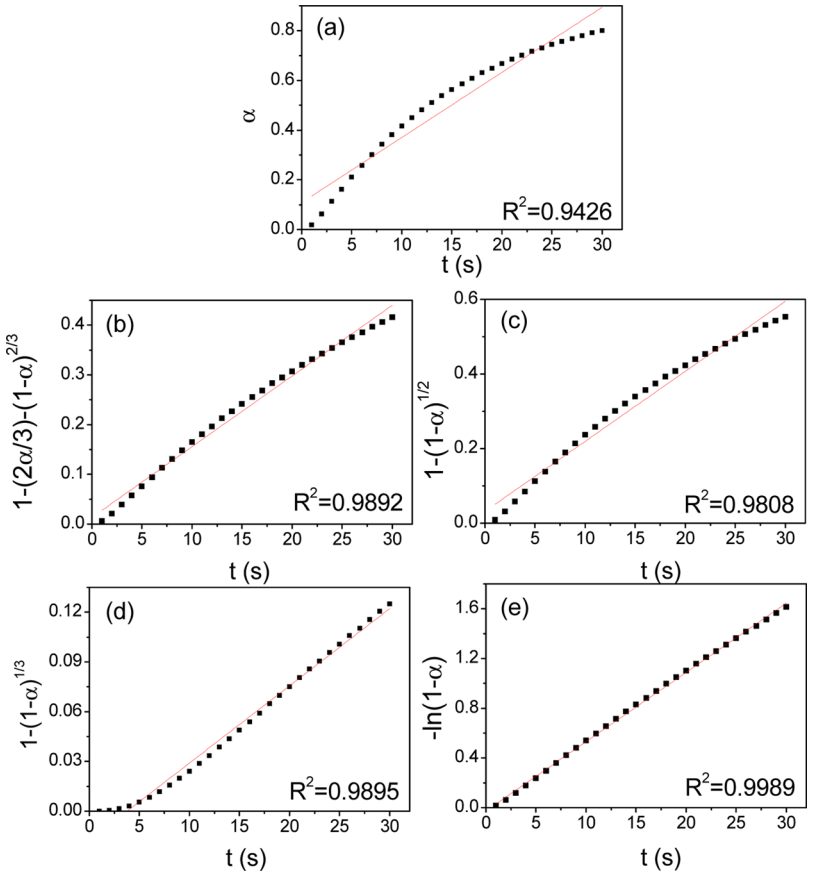

Figure 7. Kinetic models for the rehydrogenation of MgH_2−5GNSs at 300 °C: (a) chemisorption, (b) core−shell growth, (c) two-dimensional growth, (d) three-dimensional growth, (e) Mampel equation.

can be excluded, because an 1D growth mechanism could not be brought out by high-energy ball milling.[45] Therefore, to examine the mechanisms for rehydrogenation, the hydrogen absorption data ($0 \leq \alpha \leq 0.8$) at 300 °C was further fitted to different reaction models consistent with Avrami exponent $n \approx 1$ (see Supporting Information eqs 4−8 in Table S1), as shown in Figure 7. Among these reaction models, the plot of $-\ln(1-\alpha)$ against the time t gives the best fitting result ($R^2 = 0.9989$), and other reaction models have comparatively poor fits ($R^2 = 0.9426$−0.9895). The kinetic analysis result reveals that the absorption process of the MgH_2−5GNSs sample conforms to the Mampel equation formulated through the random nucleation approach. We have also presented the plots of the above conceivable mechanism against time t for the absorption process at different temperatures, as shown in Figure 8. It was found that all curves have a linear coefficient $R^2 > 0.9939$,

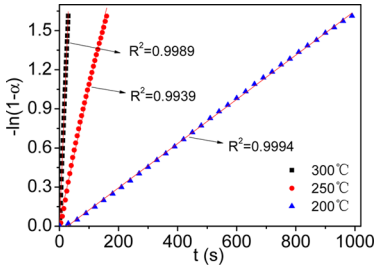

Figure 8. Kinetic model of the Mampel equation for rehydrogenation of MgH_2−5GNSs at different temperatures.

indicating that the absorption mechanism does not vary within an experimental temperature range. For dehydrogenation at 350 °C, the value of n was determined to be 1.22 (Table 2 and Figure 5b), implying that the mechanism of interface-controlled growth with grain boundary nucleation commanded the isothermal decomposition process.[41] While reducing the desorption temperature from 320 °C to 300 °C, the Avrami exponent n increases from 1.78 to 2.20, indicating that a nucleation and two-dimensional growth mechanism is suitable for the desorption process.[46]

3.3. Microstructural Characterization. Figure 9a presents the XRD patterns of MgH_2−5GNSs ball-milled for 20 h and pure-milled MgH_2 before cycling. In both samples before cycling, it was found that β-MgH_2 is the main phase and Mg is not detected, indicating that the desorbed reaction of MgH_2 does not happen during ball milling. After the sixth cycle (Figure 9b), it was clearly found that the intensity of diffraction peaks rises sharply for both MgH_2−5GNSs and pure-MgH_2 composites. Moreover, several small diffraction peaks due to Mg were observed for the pure-MgH_2 sample, and this can explain why the hydrogen storage capacity is reduced during cycling. In addition, the Sherrer equation[47] was used for estimating the grain sizes of β-MgH_2 according to the diffraction pattern (see Table S2 in Supporting Information). It was noted that the crystal size of β-MgH_2 increased from 7.3 for MgH_2−5GNSs and 10.8 nm for pure-MgH_2 before cycling to 19.5 (MgH_2−5GNSs) and 32 nm (pure-MgH_2). It was believed that GNSs can act as a crystal growth inhibitor for MgH_2−5GNSs composites during dehydrogenation/rehydrogenation cycling. It is well known that the enhanced cyclic

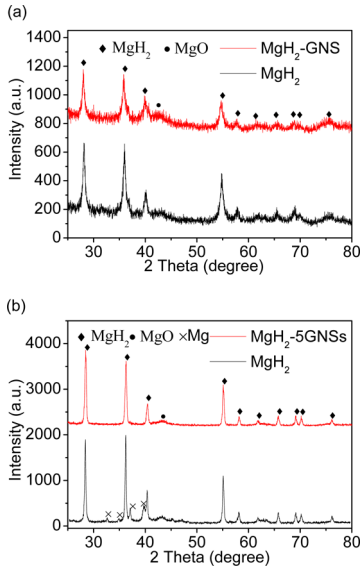

Figure 9. X-ray diffraction patterns of the MgH_2−5GNSs and MgH_2 composites (a) before and (b) after cycling.

stability and sorption kinetics can be ascribed to the smaller crystal size, which quickens the hydrogen diffusion.

In addition, TEM analysis was further performed to investigate the microstructure of the MgH_2−5GNSs composites before and after sixth cycling. It was found that both samples before and after cycling are heterogeneous and that the GNSs can be readily distinguished despite their low content and long ball milling time (Figure 10a,b). The fine grain

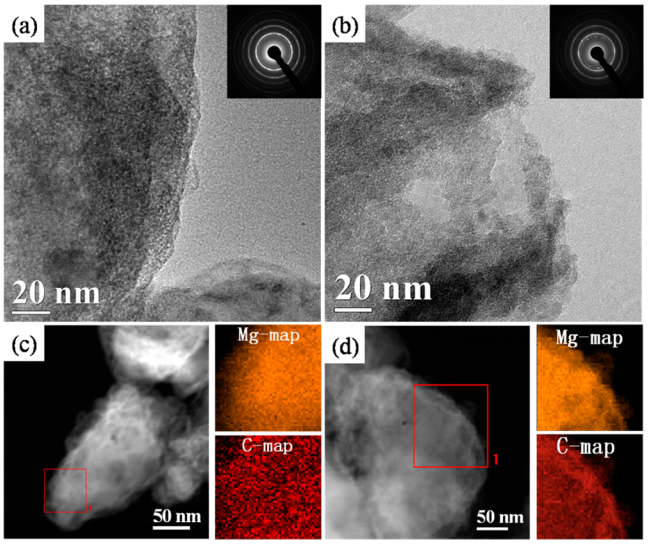

Figure 10. TEM micrographs of the MgH_2−5GNSs composites: (a) before and (b) after cyclic measurements; HAADF STEM micrographs and element mapping images of the MgH_2−5GNSs composites: (c) before and (d) after cyclic measurements. Insets in panels a and b are selected area electron diffraction (SAED) patterns.

distribution of the samples before and after cycling can also be confirmed by the corresponding SAED patterns (insets in Figure 10a,b). Both samples exhibit a completely continuous ring pattern, representing disorderly and irregular GNS dispersal in both samples and very fine grain size of the samples. To further analyze the GNS distribution in the MgH_2 matrix, STEM was used on the composites before and after cycling (Figure 10c,d). It was demonstrated that the GNSs still cover the hydride particles in both of the MgH_2−5GNSs composites before and after cycling. The region that was squared in Figure 10c,d was also studied by EDS elemental mapping. As highlighted by elemental mapping (Figure 10c,d), the GNSs cover the MgH_2 quite completely and uniformly without any detectable aggregation. Moreover, as shown by HR-TEM in Figure 11a, crystallites of MgH_2 with sizes of about

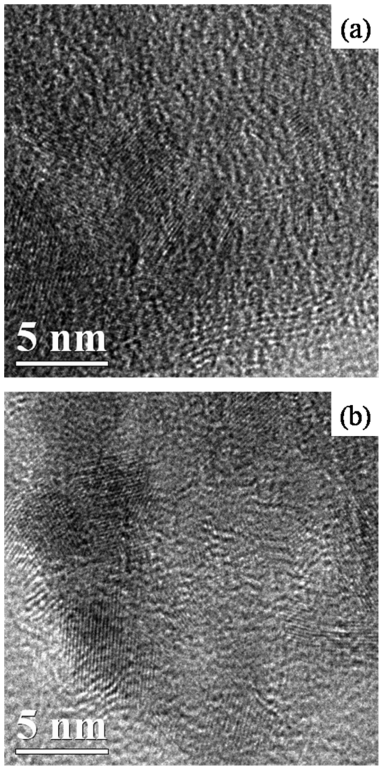

Figure 11. HR-TEM micrographs of the MgH_2−5GNSs composites: (a) before and (b) after cyclic measurements.

6−9 nm can be easily identified for the MgH_2−5GNSs composites before cycling. After the sixth cycling, the crystallite size of MgH_2−5GNSs shows a larger size of several ten nanometers compared with that before cycling (Figure 11b), which is consistent with the results from XRD. It was also found that GNS covers on the hydride are visible in both the as-milled and as-cycled composites.

The characteristic graphene peaks around 2939 cm^{-1} (D+D′), 2680 (2D), 1605 (G-band), and 1345 (D-band) are clearly shown in the Raman spectra of the composites before and after cycling (Figure 12). D and G Raman peaks can be regarded as the vibrations of sp^2-C and the disorder of the graphene edges. It was demonstrated that the defective GNSs still survive even after six dehydrogenation/rehydrogenation cycles and cover the hydride surface in a disorderly and irregular manner. It was proposed that the smaller GNSs with more defective edges can prevent hydride agglomeration and provide more active edge sites during dehydrogenation/rehydrogenation.

4. DISCUSSION

The main difference in the dehydrogenation/rehydrogenation kinetics between the MgH_2−5GNSs composites and pure-

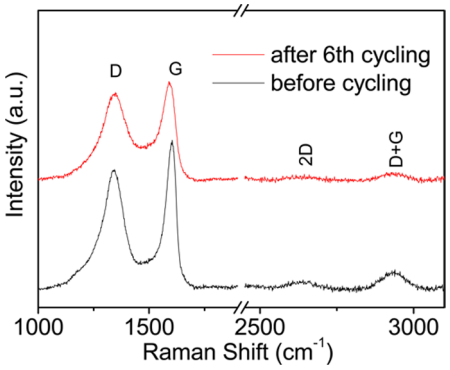

Figure 12. Raman spectra of the MgH_2−5GNSs composites before and after cyclic measurements.

milled MgH_2 powder is the effects of nanosize and defective GNSs. First, highly crumpled GNSs can act as a grain growth inhibitor to prevent Mg/MgH_2 particle coarsening during dehydrogenation/rehydrogenation processes as shown by XRD results (Figure 9) and HR-TEM (Figure 11), so as to lead to an improved kinetics performance and cyclic stability. Second, besides the particle growth inhibitive effects, GNSs can also act as a catalyst during dehydrogenation/rehydrogenation. Recent promising computational studies demonstrated that the process of H_2 dissociation can be more facile on O-doped graphene ribbon, which requires an energy of 0.47 eV for O-doped ribbon compared with 1.54 eV under normal circumstances.[48] In our work, we have provided evidence for the existence of O-doping sites in GNSs by XPS analysis (Figure 1b−d). It was possible to infer that the highly crumpled, oxygen-containing GNS ball milling with MgH_2 could provide more active catalytic defect sites to benefit H_2 surface adsorption and dissociation, thus to promote the dehydrogenation/rehydrogenation of MgH_2. Recent theoretical study has also proposed that GNSs with more active edge sites can weaken Al−H bonds during the decomposition of sodium alanate.[49] Similarly to the Al−H bonds, breaking the Mg−H bonds is the only reaction, and the dissociation of Mg−H bonds might be affected by the O-doped, highly crumpled GNSs with more active edge sites. The observation of improvement on dehydrogenation/rehydrogenation kinetics was indirect evidence for that. Third, STEM (Figure 10c,d) and HR-TEM (Figure 11) observations show that GNSs are uniformly distributed in the mixtures before and after rehydrogenation/dehydrogenation cycling and that many defects exist among the composites. So it was reasonable to propose that GNS catalysts be metal-free, contacting Mg or MgH_2 to form many lattice defects and an interphase boundary, which serves as nucleation and growth centers for MgH_2/Mg during rehydrogenation/dehydrogenation, providing channels to facilitate H atom diffusion for the MgH_2/Mg matrix. Considering that the nucleation and growth is the main rate-controlling step, we posit that in Mg−GNSs or MgH_2−GNSs composites, rapid nucleation and accumulation of H atoms occurs along these defects to form MgH_2 or Mg layers randomly followed by subsequent phase growth and thickening from the Mg or MgH_2 core.[12] Evidently, GNSs ball milled with MgH_2 as additives to produce a kinetic effect makes some difference in comparison to using other sources of carbon (CNTs, C_{60}, AC, graphite, etc.). GNSs not only act as grain growth inhibitors and nucleation and growth centers like that of other carbon sources, but they also provide more active edge sites such as zigzag or O-doped sites because of the special structure of GNSs, which was also demonstrated to be effective on the sorption properties of MgH_2.

In summary, a modeling study on the rehydrogenation/dehydrogenation of MgH_2 was performed, choosing highly crumpled, oxygen-containing GNSs as the catalyst. The results show that the rehydrogenation/dehydrogenation kinetic improvement and cyclic stability are due to the effects of highly crumpled, oxygen-containing GNSs and nanosize. It is also suggested that suitabe GNSs with special architectures and components may promise inexpensive, metal-free alternatives for metal-based catalysts, because metal-based catalysts often suffer from high cost, noxious effects on the environment, and byproducts during cycling.

5. CONCLUSIONS

The nanostructured uniform mixture of MgH_2−5GNSs powder prepared by ball milling exhibits improved dehydrogenation/rehydrogenation kinetics and cycle stability compared to pure-milled MgH_2. At 300 °C, 6.6 wt % H_2 can be absorbed within only 1 min and 6.3 wt % H_2 can be released within 80 min for MgH_2−5GNSs composites. Moreover, 5.91 wt % H_2 can be absorbed within 30 min at 200 °C. The MgH_2−5GNSs composites demonstrate a high cyclic stability with no difference in hydrogen storage capacity after six cycles of dehydrogenation/rehydrogenation. Both dehydrogenation/rehydrogenation processes comply with JMA formalism with different Avrami exponents, which presents different desorption/absorption mechanisms during dehydrogenation/rehydrogenation. Further, microstructure analysis on the milled MgH_2−5GNSs composites based on XRD, HRTEM, STEM, and Raman spectroscopy (Figure 12) reveals a grain size of 5−9 nm with uniform distribution of defective GNSs among the MgH_2 particles. It is suggested that the enhancement of the dehydrogenation/rehydrogenation kinetics and cyclic stability could be due to the coupled effects of nanosizing and the addition of defective GNSs.

■ ASSOCIATED CONTENT

Supporting Information

Different reaction models consistent with Avrami exponent $n \approx 1$ (Table S1); grain size of the MgH_2−5GNS and MgH_2 samples before and after cycling (Table S2). This material is available free of charge via the Internet at http://pubs.acs.org.

■ AUTHOR INFORMATION

Corresponding Author

*E-mail: wangyj@nankai.edu.cn.

Notes

The authors declare no competing financial interest.

■ ACKNOWLEDGMENTS

This work was financially supported by Qualified Personnel Foundation of Taiyuan University of Technology (QPFT, tyutrc-201355a), NSFC (5117108), MOST project (2010CB631303, 2012AA051901), MOE (IRT-13R30), and 111Project (B12015).

■ REFERENCES

(1) Schlapbach, L.; Zuttel, A. Hydrogen-Storage Materials for Mobile Applications. *Nature* **2001**, *414*, 353−358.

(2) Grochala, W.; Edwards, P. P. Thermal Decomposition of the Non-Interstitial Hydrides for the Storage and Production of Hydrogen. *Chem. Rev.* **2004**, *104*, 1283−1316.
(3) Chen, P.; Zhu, M. Recent Progress in Hydrogen Storage. *Mater. Today* **2008**, *11*, 36−43.
(4) Eberle, U.; Felderhoff, M.; Schuth, F. Chemical and Physical Solutions for Hydrogen Storage. *Angew. Chem., Int. Ed.* **2009**, *48*, 6608−6630.
(5) Yang, J.; Sudik, A.; Wolverton, C.; Siegel, D. J. High Capacity Hydrogen Storage Materials: Attributes for Automotive Applications and Techniques for Materials Discovery. *Chem. Soc. Rev.* **2010**, *39*, 656−675.
(6) Cheng, F.; Tao, Z.; Liang, J.; Chen, J. Efficient Hydrogen Storage with the Combination of Lightweight Mg/MgH_2 and Nanostructures. *Chem. Commun.* **2012**, *48*, 7334−7343.
(7) Sakintuna, B.; Lamari-Darkrim, F.; Hirscher, M. Metal Hydride Materials for Solid Hydrogen Storage: A Review. *Int. J. Hydrogen Energy* **2007**, *32*, 1121−1140.
(8) Hanada, N.; Ichikawa, T.; Fujii, H. Catalytic Effect of Nanoparticle 3d-Transition Metals on Hydrogen Storage Properties in Magnesium Hydride MgH_2 Prepared by Mechanical Milling. *J. Phys. Chem. B* **2005**, *109*, 7188−7194.
(9) Aguey-Zinsou, K. F.; Ares Fernandez, J. R.; Klassen, T.; Bormann, R. Effect of Nb_2O_5 On MgH_2 Properties during Mechanical Milling. *Int. J. Hydrogen Energy* **2007**, *32*, 2400−2407.
(10) Zhang, J.; Cuevas, F.; Zaïdi, W.; Bonnet, J.-P.; Aymard, L.; Bobet, J.-L.; Latroche, M. Highlighting of a Single Reaction Path during Reactive Ball Milling of Mg and TM by Quantitative H_2 Gas Sorption Analysis To Form Ternary Complex Hydrides (TM = Fe, Co, Ni). *J. Phys. Chem. C* **2011**, *115*, 4971−4979.
(11) Nielsen, T. K.; Besenbacher, F.; Jensen, T. R. Nanoconfined Hydrides for Energy Storage. *Nanoscale* **2011**, *3*, 2086−2098.
(12) Jeon, K.-J.; Moon, H. R.; Ruminski, A. M.; Jiang, B.; Kisielowski, C.; Bardhan, R.; Urban, J. J. Air-Stable Magnesium Nanocomposites Provide Rapid and High-Capacity Hydrogen Storage without Using Heavy-Metal Catalysts. *Nat. Mater.* **2011**, *10*, 286−290.
(13) Zheng, S.; Li, Z. P.; Bendersky, L. A. Understanding the Role of Vanadium in Enhancing the Low-Temperature Hydrogenation Kinetics of a Mg Thin Film. *ACS Appl. Mater. Interfaces* **2013**, *5*, 6968−74.
(14) Imamura, H.; Takesue, Y.; Tabata, S.; Shigetomi, N.; Sakata, Y.; Tsuchiya, S. Hydrogen Storage Composites Obtained by Mechanical Grinding of Magnesium with Graphite Carbon. *Chem. Commun.* **1999**, 2277−2278.
(15) Verón, M. G.; Troiani, H.; Gennari, F. C. Synergetic Effect of Co and Carbon Nanotubes on MgH_2 Sorption Properties. *Carbon* **2011**, *49*, 2413−2423.
(16) Wu, C. Z.; Wang, P.; Yao, X.; Liu, C.; Chen, D. M.; Lu, G. Q.; Cheng, H. M. Effect of Carbon/Noncarbon Addition on Hydrogen Storage Behaviors of Magnesium Hydride. *J. Alloys Compd.* **2006**, *414*, 259−264.
(17) Lillo-Ródenas, M.; Guo, Z.; Aguey-Zinsou, K.; Cazorla-Amorós, D.; Linares-Solano, A. Effects of Different Carbon Materials on MgH_2 Decomposition. *Carbon* **2008**, *46*, 126−137.
(18) Amirkhiz, B. S.; Danaie, M.; Barnes, M.; Simard, B.; Mitlin, D. Hydrogen Sorption Cycling Kinetic Stability and Microstructure of Single-Walled Carbon Nanotube (SWCNT) Magnesium Hydride (MgH_2) Nanocomposites. *J. Phys. Chem. C* **2010**, *114*, 3265−3275.
(19) Jia, Y.; Guo, Y.; Zou, J.; Yao, X. Hydrogenation/Dehydrogenation in MgH_2-Activated Carbon Composites Prepared by Ball Milling. *Int. J. Hydrogen Energy* **2012**, *37*, 7579−7585.
(20) Imamura, H.; Kusuhara, M.; Minami, S.; Matsumoto, M.; Masanari, K.; Sakata, Y.; Itoh, K.; Fukunaga, T. Carbon Nanocomposites Synthesized by High-Energy Mechanical Milling of Graphite and Magnesium for Hydrogen Storage. *Acta Mater.* **2003**, *51*, 6407−6414.
(21) Imamura, H.; Tabata, S.; Takesue, Y.; Sakata, Y.; Kamazaki, S. Hydriding−Dehydriding Behavior of Magnesium Composites Obtained by Mechanical Grinding with Graphite Carbon. *Int. J. Hydrogen Energy* **2000**, *25*, 837−843.
(22) Imamura, H.; Sakasai, N.; Fujinaga, T. Characterization and Hydriding Properties of Mg-Graphite Composites Prepared by Mechanical Grinding as New Hydrogen Storage Materials. *J. Alloys Compd.* **1997**, *253*−*254*, 34−37.
(23) Novoselov, K. S.; Geim, A. K.; Morozov, S. V.; Jiang, D.; Katsnelson, M. I.; Grigorieva, I. V.; Dubonos, S. V.; Firsov, A. A. Two-Dimensional Gas of Massless Dirac Fermions in Graphene. *Nature* **2005**, *438*, 197−200.
(24) Geim, A. K.; Novoselov, K. S. The Rise of Graphene. *Nat. Mater.* **2007**, *6*, 183−191.
(25) Saravanakumar, B.; Purushothaman, K. K.; Muralidharan, G. Interconnected V_2O_5 Nanoporous Network for High-Performance Supercapacitors. *ACS Appl. Mater. Interfaces* **2012**, *4*, 4484−90.
(26) Wu, Z.-S.; Ren, W.; Wen, L.; Gao, L.; Zhao, J.; Chen, Z.; Zhou, G.; Li, F.; Cheng, H.-M. Graphene Anchored with Co_3O_4 Nanoparticles as Anode of Lithium Ion Batteries with Enhanced Reversible Capacity and Cyclic Performance. *ACS Nano* **2010**, *4*, 3187−3194.
(27) Tao, S.; Yue, W.; Zhong, M.; Chen, Z.; Ren, Y. Fabrication of Graphene-Encapsulated Porous Carbon−Metal Oxide Composites as Anode Materials for Lithium-Ion Batteries. *ACS Appl. Mater. Interfaces* **2014**, *6*, 6332−6339.
(28) Peining, Z.; Nair, A. S.; Shengjie, P.; Shengyuan, Y.; Ramakrishna, S. Facile Fabrication of TiO_2−Graphene Composite with Enhanced Photovoltaic and Photocatalytic Properties by Electrospinning. *ACS Appl. Mater. Interfaces* **2012**, *4*, 581−585.
(29) Jiao, Y.; Zheng, Y.; Jaroniec, M.; Qiao, S. Z. Origin of the Electrocatalytic Oxygen Reduction Activity of Graphene-Based Catalysts: A Roadmap To Achieve the Best Performance. *J. Am. Chem. Soc.* **2014**, *136*, 4394−4403.
(30) Bo, X.; Han, C.; Zhang, Y.; Guo, L. Confined Nanospace Synthesis of Less Aggregated and Porous Nitrogen-Doped Graphene as Metal-Free Electrocatalysts for Oxygen Reduction Reaction in Alkaline Solution. *ACS Appl. Mater. Interfaces* **2014**, *6*, 3023−3030.
(31) Eda, G.; Chhowalla, M. Graphene-Based Composite Thin Films for Electronics. *Nano Lett.* **2009**, *9*, 814−818.
(32) Nguyen, K. T.; Zhao, Y. Integrated Graphene/Nanoparticle Hybrids For Biological and Electronic Applications. *Nanoscale* **2014**, *6*, 6245−6266.
(33) Mondal, T.; Bhowmick, A. K.; Krishnamoorti, R. Stress Generation and Tailoring of Electronic Properties of Expanded Graphite by Click Chemistry. *ACS Appl. Mater. Interfaces* **2014**, *6*, 7244−7253.
(34) Liu, G.; Wang, Y.; Qiu, F.; Li, L.; Jiao, L.; Yuan, H. Synthesis of Porous Ni@rGO Nanocomposite and Its Synergetic Effect on Hydrogen Sorption Properties of MgH_2. *J. Mater. Chem.* **2012**, *22*, 22542−22549.
(35) Liu, G.; Wang, Y.; Jiao, L.; Yuan, H. Solid-State Synthesis of Amorphous TiB_2 Nanoparticles on Graphene Nanosheets with Enhanced Catalytic Dehydrogenation of MgH_2. *Int. J. Hydrogen Energy* **2014**, *39*, 3822−3829.
(36) Liu, G.; Wang, Y.; Xu, C.; Qiu, F.; An, C.; Li, L.; Jiao, L.; Yuan, H. Excellent Catalytic Effects of Highly Crumpled Graphene Nanosheets on Hydrogenation/Dehydrogenation of Magnesium Hydride. *Nanoscale* **2013**, *5*, 1074−81.
(37) Stampfer, J. F.; Holley, C. E.; Suttle, J. F. The Magnesium-Hydrogen System. *J. Am. Chem. Soc.* **1960**, *82*, 3504−3508.
(38) Fernández, J. F.; Sánchez, C. R. Rate Determining Step in the Absorption and Desorption of Hydrogen by Magnesium. *J. Alloys Compd.* **2002**, *340*, 189−198.
(39) Rudman, P. Hydrogen-Diffusion-Rate-Limited Hydriding and Dehydriding Kinetics. *J. Appl. Phys.* **1979**, *50*, 7195−7199.
(40) Norberg, N. S.; Arthur, T. S.; Fredrick, S. J.; Prieto, A. L. Size-Dependent Hydrogen Storage Properties of Mg Nanocrystals Prepared from Solution. *J. Am. Chem. Soc.* **2011**, *133*, 10679−10681.
(41) Zahiri, B.; Danaie, M.; Tan, X.; Amirkhiz, B. S.; Botton, G. A.; Mitlin, D. Stable Hydrogen Storage Cycling in Magnesium Hydride, in the Range of Room Temperature to 300 °C, Achieved Using a New

Bimetallic Cr-V Nanoscale Catalyst. *J. Phys. Chem. C* **2011**, *116*, 3188−3199.
(42) Mao, J. F.; Guo, Z. P.; Yu, X. B.; Liu, H. K.; Wu, Z.; Ni, J. Enhanced Hydrogen Sorption Properties of Ni and Co-Catalyzed MgH_2. *Int. J. Hydrogen Energy* **2010**, *35*, 4569−4575.
(43) Gerard, N. Role of Nucleation in Some Hydride Formation Kinetics. *J. Less-Common Met.* **1987**, *131*, 13−23.
(44) Avrami, M. Kinetics of Phase Change. I. General Theory. *J. Chem. Phys.* **1939**, *7*, 1103−1112.
(45) Suryanarayana, C. Mechanical Alloying and Milling. *Prog. Mater. Sci.* **2001**, *46*, 1−184.
(46) Liang, G.; Huot, J.; Boily, S.; Schulz, R. Hydrogen Desorption Kinetics of A Mechanically Milled MgH_2+5 atom %V Nanocomposite. *J. Alloys Compd.* **2000**, *305*, 239−245.
(47) Patterson, A. L. The Scherrer Formula for X-Ray Particle Size Determination. *Phys. Rev.* **1939**, *56*, 978−982.
(48) Liao, T.; Sun, C.; Sun, Z.; Du, A.; Smith, S. Chemically Modified Ribbon Edge Stimulated H_2 Dissociation: A First-Principles Computational Study. *Phys. Chem. Chem. Phys.* **2013**, *15*, 8054−8057.
(49) Qian, Z.; Hudson, M. S. L.; Raghubanshi, H.; Scheicher, R. H.; Pathak, B.; Araújo, C. M.; Blomqvist, A.; Johansson, B.; Srivastava, O. N.; Ahuja, R. Excellent Catalytic Effects of Graphene Nanofibers on Hydrogen Release of Sodium Alanate. *J. Phys. Chem. C* **2012**, *116*, 10861−10866.